Numerical Optimization of Nozzle Shapes for Fused Deposition Modeling

Steffen Tillmann[1*], Felipe A. González[1] and Stefanie Elgeti[1,2]

[1*]Chair for Computational Analysis of Technical Systems, RWTH Aachen University, Schinkelstraße 2, Aachen, 52062, Germany.
[2]Institute of Lightweight Design and Structural Biomechanics, TU Wien, Gumpendorfer Straße 7, Vienna, A-1060, Austria,.

*Corresponding author(s). E-mail(s): tillmann@cats.rwth-aachen.de;
Contributing authors: gonzalez@cats.rwth-aachen.de;
stefanie.elgeti@tuwien.ac.at;

Abstract

Purpose: In fused deposition modeling (FDM), the nozzle plays a critical role in enabling high printing speeds while maintaining precision. Despite its importance, most applications still rely on standard nozzle designs. This work investigates the influence of nozzle geometry on pressure loss inside the nozzle, a key factor in high-speed printing performance.

Design/methodology/approach: We focus on optimizing the nozzle shape to minimize the pressure loss and establish a framework that allows both simple angle-based optimization and more advanced spline-based parametrization. To model the polymer melt flow, we compare two constitutive descriptions commonly employed in the literature: a temperature-dependent, shear-thinning viscous model and an isothermal viscoelastic model.

Findings: For the viscous model, the optimal half-opening angle exhibits a strong dependence on the feeding rate, with higher rates favoring half-opening angles near 30°, whereas lower rates are more efficient at larger angles. In contrast, the viscoelastic model predicts a weaker dependence of the optimal angle on the feeding rate. For both models, spline-based parametrization yields only marginal improvements over angle optimization in terms of reducing pressure loss.

Originality/value: This paper presents a comparative study of FDM nozzle shape optimization using different simulation models. We introduce a flexible optimization framework that accommodates both simple and advanced geometric parametrizations. The results highlight the impact of model choice on the optimal nozzle geometry and provide support for improving nozzle design in

high-speed printing applications.

Keywords: Fused deposition modeling, 3D Printing Nozzle, Shape optimization, Finite element method

1 Introduction

With recent technological advances, 3D printing has become a more commonly used manufacturing technique in many fields. While it was initially employed primarily for prototyping, it is now also used for the production of final parts. Among 3D printing technologies, Fused Deposition Modeling (FDM) is particularly widely used due to its low cost, ease of operation, and broad material availability. (Paul, 2021; Cano-Vicent *et al.*, 2021) In the initial stage of FDM, the thermoplastic filament is driven into the hotend by feed rollers, where it is heated above its glass transition and melting temperatures. The polymer transitions into a viscoelastic melt and is forced through a convergent nozzle, where the reduction in cross-section induces an increase in flow velocity and shear rate. Upon deposition onto the build plate, the extrudate undergoes rapid cooling and solidification, governed by heat conduction to the substrate and convective heat transfer to the surrounding environment (Hiemenz, 2011). The most commonly used materials are polymers, but other materials such as metals or ceramics are possible (Solomon *et al.*, 2021). In this paper, we will focus only on polymers. To reduce manufacturing costs, printing time must be minimized by increasing the printing speed. However, higher printing speeds result in greater pressure losses within the nozzle, which in turn demand higher feeding forces on the filament (Schuller *et al.*, 2024b; Haleem *et al.*, 2017). Higher printing speeds can furthermore adversely influence the mechanical properties of the produced parts (Žarko *et al.*, 2017; Miazio, 2019; Ansari and Kamil, 2021).

One approach to improve the printing quality is to optimize the process parameters. In (Shirmohammadi *et al.*, 2021; Pereira *et al.*, 2023), parameters such as nozzle temperature, layer thickness, printing speed, and nozzle diameter were optimized to improve the mechanical properties of the produced part, such as reducing surface roughness. Further studies have focused on optimizing printing speed (Mushtaq *et al.*, 2023) or on performing multi-objective optimization (Nguyen *et al.*, 2020).

Most of the aforementioned studies rely on experimental investigations. However, simulations are essential for understanding polymer melt flow in the nozzle, since obtaining high-resolution flow field measurements inside the nozzle is not feasible. Several works have simulated the flow field within the nozzle (Nzebuka *et al.*, 2022b; Hofstaetter *et al.*, 2015; Hajili and Temirel, 2024), while others combined simulations with experimental validation (Hıra *et al.*, 2022). In (Serdeczny *et al.*, 2020b), experimental measurements of feeding force and pressure loss under different operating conditions were compared against analytical models.

The performed studies have mainly focused on determining the thermofluidic characteristics of the polymer melt, such as temperature distributions and pressure drop, at

the first stage of FDM. These quantities are relevant in the following way: At high extrusion speed, an uneven temperature at the nozzle exit would lead to insufficient melting and a potential risk of clogging. Furthermore, the pressure drop is directly correlated to the feeding force, which ultimately determines the maximum manufacturing speed (Xu *et al.*, 2023).

In literature, the molten polymer is commonly modeled as a generalized Newtonian fluid (GNF) with a time-temperature superposition approach, which accounts for the temperature-dependent viscosity and shear-thinning behavior (Serdeczny *et al.*, 2020a; Zhang *et al.*, 2023; Pigeonneau *et al.*, 2020; Nzebuka *et al.*, 2022a; Ufodike and Nzebuka, 2022; Marion *et al.*, 2023, 2024). The GNF model proved to be efficient and accurate in predicting the thermofluid flow inside the hotend at different feeding rates. However, other researchers prefer viscoelastic models, as these not only describe the viscous flow behavior but also capture the elastic memory effects of polymer melts. Such models are better suited for representing stress relaxation, strain history, and non-linear flow responses, which are important for accurately predicting nozzle flow characteristics (Schuller *et al.*, 2024a; Phan *et al.*, 2020; Serdeczny *et al.*, 2022; Xu *et al.*, 2024). The Weissenberg number (Wi) is used to compare the elastic forces to the viscous forces. Reported Weissenberg numbers range from 0.02 to 0.8 at different feeding rates (Pigeonneau *et al.*, 2020; Marion *et al.*, 2023), which are relatively low. Nevertheless, because the polymer melt within the nozzle is dominated by elongational flow, viscoelastic models remain more suitable for accurately capturing the flow behavior. With respect to the pressure loss, it can be observed that most losses occur within the nozzle since the losses through the liquefier are usually insignificant due to its larger diameter (Phan *et al.*, 2020). When GNF and viscoelastic models were compared, the viscoelastic model was shown to be more accurate in predicting the pressure drop in the nozzle and the feeding force (Serdeczny *et al.*, 2022). Viscoelastic flow can also capture elastic instabilities, resulting in increased pressure drops and the formation of recirculation zones along the nozzle walls upstream (Schuller *et al.*, 2022). The presence of such upstream vortices would lead to an inhomogeneous melting distribution, increasing the risk of clogging, as unmelted material could reach the nozzle contraction. An aspect not fully studied is how the nozzle geometry affects the flow patterns and the pressure drop. However, the assumption of isothermal flow neglects crucial melting effects and the constantly evolving thermofluid properties of the polymer melt within the hotend.

Regarding the modeling of the melting process, the enthalpy-porosity method has been used (Nzebuka *et al.*, 2022a; Ufodike and Nzebuka, 2022; Xu *et al.*, 2024) to model the phase change during melting. Even though the method originated from the alloy solidification process, it has also been validated in polymer melting (Xu *et al.*, 2024). This technique models the phase-transition interface as an equivalent porous medium, where the porosity represents the ratio of the latent heat content of a cell to the latent heat of fusion. This interface is commonly referred to as the mushy zone. The solid behavior is achieved by introducing a Darcy force source term into the momentum equation that works as a penalty-like term on the velocity. The enthalpy-porosity model effectively simulates the melting process without adding further complexity to

the framework (Xu *et al.*, 2024). However, some authors have shown that the melting enthalpy is negligible (Phan *et al.*, 2020; Zhang *et al.*, 2023; Marion *et al.*, 2024). In fact, under typical 3D printing conditions, the heat flow to melt the polymer is relatively small, accounting for up to 5% of the total heating (Marion *et al.*, 2024). Therefore, the contributions of crystallization and fusion effects can be neglected (Phan *et al.*, 2020). Yet, the phase-change interface remains crucial, as it indicates when unmelted material approaches the nozzle contraction. Additionally, when a viscoelastic model was used, it was shown that the stress formation starts immediately after the phase-change interface within the hotend (Xu *et al.*, 2024). As an alternative to the porosity method, the temperature-dependent viscosity model can be used to capture the mushy zone as viscosity increases at lower temperatures. Simulations indicate that the temperature became less homogeneous at higher flow rates, leading to a lower extrusion temperature (Zhang *et al.*, 2023). Consequently, the non-isothermal aspect of the polymer melt cannot be overlooked because low extrusion temperatures result in high-pressure drops (Serdeczny *et al.*, 2020a), limiting the printing speed and increasing the risk of clogging.

The complexity of the thermofluidic behavior of the polymer melt is also reflected by a strongly inhomogeneous shear rate distribution within the nozzle. In particular, a spike in the shear rate is observed along the wall of the nozzle tip, leading to a localized stress concentration (Phan *et al.*, 2020). This effect is intensified as the feeding rate increases, leading to larger stresses in the extruded filament. This exhibits the fact that stress formation, initiated after melting at the hotend, continues during extrusion, and its understanding is crucial for predicting the shape-morphing mechanism of the final part.

As mentioned above, the nozzle plays a crucial part in the process of FDM. The influence of the diameter and temperature of the nozzle was investigated in (Kedare *et al.*, 2020). In (Wang *et al.*, 2025), the contraction angle of the nozzle and the process parameters were optimized together. As mentioned before, pressure loss is essential for high printing speeds. In (Haleem *et al.*, 2017), the pressure losses were compared for different contraction angles and outlet diameters.

A recent study on the shape optimization of the nozzle geometry using an isothermal viscoelastic fluid has been carried out (Schuller *et al.*, 2024b). The study demonstrated how the optimal nozzle profile varies for different polymer materials. The nozzle shape was optimized to minimize pressure loss using a spline-based parametrization, which provides greater flexibility in shaping the nozzle. In this paper, we extend this approach by optimizing the nozzle shape for different feeding rates and outlet diameters. Our procedure first optimizes the contraction angle and subsequently employs a spline-based parametrization to determine the overall optimal nozzle geometry.

In general, shape optimization methods can be split into two groups regarding the geometry representation: parametric (Azegami *et al.*, 2020; Chapelier *et al.*, 2022) or nonparametric (Hojjat *et al.*, 2014; Giannakoglou and Papadimitriou, 2008; Jameson, 2003; Le *et al.*, 2011). In the case of nonparametric shape optimization, a simulation model capable of the adjoint method is required to compute the shape derivatives of all mesh nodes in a feasible computational time. In cases where the simulation models

do not provide objective function derivatives, the only feasible methods are the parametric shape optimization methods, which provide a low-dimensional representation of the geometry (Azegami *et al.*, 2020). One popular method is free-form deformation (Sederberg and Parry, 1986), where the geometry is embedded into a box spline, and the control points of the spline serve as the optimization parameters. For simpler geometries, it is possible to parametrize the geometry with a spline directly (Han and Zingg, 2014; Painchaud-Ouellet *et al.*, 2006; Schuller *et al.*, 2024b). This has the advantage that the spline is better fitted to the geometry and thus allows a more fine-tuned adaptation of the geometry, which is possible for the nozzle geometry.
Also, an appropriate optimization algorithm needs to be chosen. In cases where the simulation model does not provide derivatives, derivative-free optimization algorithms are typically used. These algorithms are, for example, explained in (Larson *et al.*, 2019; Conn *et al.*, 2009; Rios and Sahinidis, 2013). This paper will use the COBYQA algorithm (Ragonneau, 2022; Ragonneau and Zhang, 2024), a trust-region method that can handle all types of constraints.
Our paper contributes to a deeper understanding of the flow field and pressure losses within the nozzle for FDM 3D printing applications. We compute the optimal nozzle shape for different operating conditions to minimize pressure loss and provide a general framework for shape optimization that can be applied to any simulation model. The paper is structured as follows: Section 2 describes the simulation models and the nozzle geometry, and we employ two different models to compare their effects on nozzle flow. This is followed by a description of our shape optimization framework in Section 3, with the results of the numerical experiments presented in Section 4. Finally, we conclude with a summary, discussion, and outlook.

2 Simulation Model

2.1 Governing Equations

The governing equations for the two material models employed in this study are presented in the following section. Both models are formulated on the basis of the steady, incompressible Navier–Stokes equations. For a spatial domain Ω, the governing equations of momentum and mass conservation are expressed as:

$$\rho \mathbf{u} \cdot \nabla \mathbf{u} - \nabla \cdot \boldsymbol{\sigma} = \mathbf{b} \quad \text{in} \quad \Omega, \tag{1}$$

$$\nabla \cdot \mathbf{u} = 0 \quad \text{in} \quad \Omega, \tag{2}$$

with the density ρ, velocity $\mathbf{u}$, external force $\mathbf{b}$, and Cauchy stress tensor $\boldsymbol{\sigma}$. The components of the Cauchy stress tensor depend on the material model.

2.1.1 Temperature Dependent Viscous Model

For the temperature-dependent viscous model, we employ the strongly coupled, steady, incompressible Navier–Stokes equations together with the heat equation. Implementation details, including stabilization techniques, are provided in (González *et al.*, 2023; González, 2023). We use the Galerkin/least-squares stabilization to stabilize the finite

element method. In the following, the governing equations are briefly summarized. The Cauchy stress tensor in Eq. 1 consists of a hydrostatic term and a viscous term denoted as $\boldsymbol{\sigma}_\mathrm{s}$:

$$\boldsymbol{\sigma} = -p\mathbf{I} + \boldsymbol{\sigma}_\mathrm{s} = -p\mathbf{I} + 2\eta\varepsilon(\mathbf{u}). \tag{3}$$

Here, p is the pressure, η is the dynamic viscosity, and ε is the strain rate tensor $\varepsilon(\mathbf{u}) = \frac{1}{2}\left(\nabla\mathbf{u} + \nabla\mathbf{u}^\mathrm{T}\right)$. For calculating the temperature T, we use the heat equation:

$$\rho c_p \mathbf{u}\cdot\nabla T - \kappa\Delta T - 2\eta\nabla\mathbf{u} : \varepsilon(\mathbf{u}) = 0 \quad \text{in} \quad \Omega, \tag{4}$$

with the thermal conductivity κ and the specific heat capacity c_p. A generalized Newtonian model is employed to represent the behavior of polymers, specifically capturing their shear-thinning characteristics. In our model the viscosity η depends on the shear rate $\dot{\gamma} = \sqrt{2\varepsilon(\mathbf{u}) : \varepsilon(\mathbf{u})}$. We employ the Cross model to describe this shear-thinning behavior:

$$\eta(\dot{\gamma}, T) = \frac{\eta_0}{1 + \left(\frac{\eta_0\dot{\gamma}}{\tau^*}\right)^{1-n}}. \tag{5}$$

Here, η_0 is the zero-shear viscosity, τ^* is the critical shear stress, and n is the power-law index. To account for the temperature dependence, the WLF correction is used:

$$\eta_0(T) = D_1 \exp\left[-\frac{A_1\left(T - T_\mathrm{ref}\right)}{A_2 + \left(T - T_\mathrm{ref}\right)}\right], \tag{6}$$

with the viscosity D_1 at the reference temperature T_{ref}, and the parameters A_1 and A_2 specifying the temperature dependence.

2.1.2 Isothermal Viscoelastic Model

To describe viscoelastic material behaviour, we employ the incompressible Navier-Stokes equations in conjunction with the Giesekus model: The model is briefly outlined below, while implementation details, including stabilization, can be found in (Wittschieber *et al.*, 2022; Wittschieber). We use the algebraic sub-grid scale method to stabilize the finite element method for viscoelastic flow. The Cauchy stress tensor in Eq. 1 consists of a hydrostatic and a viscous term and now in addition the viscoelastic stress $\boldsymbol{\sigma}_\mathrm{p}$:

$$\boldsymbol{\sigma} = -p\mathbf{I} + 2\eta_\mathrm{s}\varepsilon(\mathbf{u}) + \boldsymbol{\sigma}_\mathrm{p}. \tag{7}$$

Here, p is the pressure, η_s is the solvent viscosity, and ε is the strain rate tensor $\varepsilon(\mathbf{u}) = \frac{1}{2}\left(\nabla\mathbf{u} + \nabla\mathbf{u}^\mathrm{T}\right)$. The viscoelastic stress is computed with the Giesekus model as the constituive relation:

$$\lambda\left(\mathbf{u}\cdot\nabla\boldsymbol{\sigma}_\mathrm{p} - \nabla\mathbf{u}\cdot\boldsymbol{\sigma}_\mathrm{p} - \boldsymbol{\sigma}_\mathrm{p}\cdot(\nabla\mathbf{u})^\mathrm{T}\right) + \boldsymbol{\sigma}_\mathrm{p} + \frac{\alpha_G\lambda}{\eta_\mathrm{p}}\boldsymbol{\sigma}_\mathrm{p}\cdot\boldsymbol{\sigma}_\mathrm{p} = 2\eta_\mathrm{p}\varepsilon(\mathbf{u}) \quad \text{in} \quad \Omega, \tag{8}$$

with the relaxation time λ, the mobility factor α_G, and polymeric viscosity η_p. In our implementation we specify the total viscosity η and the solvent viscosity ratio β:

$$\eta = \eta_\mathrm{s} + \eta_\mathrm{p}, \tag{9}$$

$$\beta = \frac{\eta_{\mathrm{s}}}{\eta_{\mathrm{p}}}. \tag{10}$$

2.2 Geometry and Boundary Conditions

In Fig. 1, the geometry of the nozzle is shown. We use a standard nozzle geometry. The specific values for each length are given in Table 1. The following boundary conditions are prescribed: In all cases, we set a uniform inlet velocity u_{in}, also called the feeding rate. In case of the viscous model, for a certain portion of the wall, L_{heat}, we set a fixed temperature T_{wall}. In the viscoelastic model, no heated wall is considered, and the fluid stresses are prescribed as zero at the inlet. At the outlet, we set the velocity in the y-direction to zero.

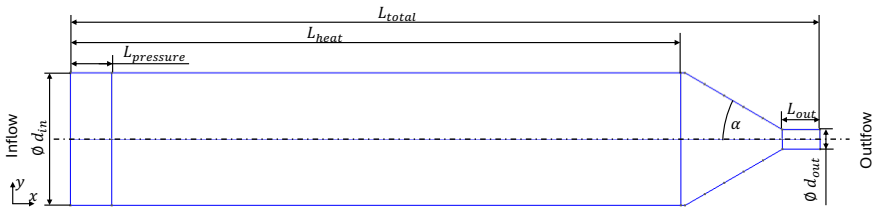

Fig. 1: Nozzle geometry. Source: Authors own work

Table 1: Geometry parameters used for the numerical experiments

Parameter	Value	Unit
L_{total}	18	mm
L_{heat}	14.66	mm
L_{out}	0.9	mm
$L_{pressure}$	1	mm
d_{in}	3.2	mm
d_{out}	0.5	mm

3 Shape Optimization Approach

The objective of the shape optimization is to reduce the feeding force by minimizing the pressure loss. To this end, the average pressure is computed at both the inlet and the outlet, and the difference is taken as the pressure loss. Specifically, the pressure at each section is obtained by averaging over its cross-sectional area. At the inlet,

the pressure is evaluated slightly downstream, at a distance $L_{pressure}$ from the actual boundary, in order to obtain more consistent values and to avoid disturbances induced by the inflow condition. Our objective function reads:

$$J = p_{inlet} - p_{outlet} = \Delta p \,, \tag{11}$$

Each average pressure value is computed by integrating the pressure over the corresponding cross-sectional area and normalizing by the area size. To facilitate comparison across different operating conditions, we additionally define the relative improvement in pressure loss, computed with respect to the initial geometry featuring a 30° contraction angle.

$$\text{relative improvement} = 1 - \frac{\Delta p(\text{optimized shape})}{\Delta p(30^\circ \text{ angle})} \,, \tag{12}$$

We employ parametric shape optimization for two main reasons: it ensures computational efficiency by keeping the number of parameters low, and it incorporates manufacturing constraints. To minimize production costs, the geometry should remain as simple as possible; therefore, in the first step, we restrict the optimization to the contraction angle α (Fig. 2a).
To investigate whether increased shape flexibility can lead to improved nozzle designs, we subsequently introduce a spline-based parametrization. A spline parametrization allows for more complex shapes at the cost of higher complexity in the nozzle's manufacturing process. The spline parametrization furthermore introduces new challenges for shape optimization. Not only is there a strong increase in computational complexity due to the much larger number of parameters, but if all control points can move freely in the x- and y-directions, the control points can easily overlap and entangle the mesh. There are different techniques to prevent mesh entangling, such as using different types of constraints. In our case, we restrict the individual movement of the control points in the x-direction. All control points' x-coordinates are controlled by a single parameter that controls the contraction angle, and only the y-coordinates can vary individually (Fig. 2b). In this way, we simultaneously reduced the degrees of freedom to save computational time while ensuring that the mesh remained well-behaved and free of entanglement. Preliminary tests indicated that this approach significantly lowered computational cost while still providing sufficient flexibility in the design, compared to allowing all control points to move in both coordinate directions.
One challenge remains: We need a monotonic decrease in the contraction to maintain reasonable manufacturability. For this, we added an inequality constraint: the y-coordinate of each subsequent control point in the x-direction has to be lower than the previous one.
The optimization loop then works as follows. First, the 2D geometry for our axisymmetric simulation model is created according to the initial values of the parametrization. We use the meshing software Gmsh (Geuzaine and Remacle, 2009) to create the parametrized geometry and mesh it. We then run the flow simulation with our in-house finite element solver, XNS. Then the pressure values are computed for the objective function, and as optimization algorithm, we use the COBYQA

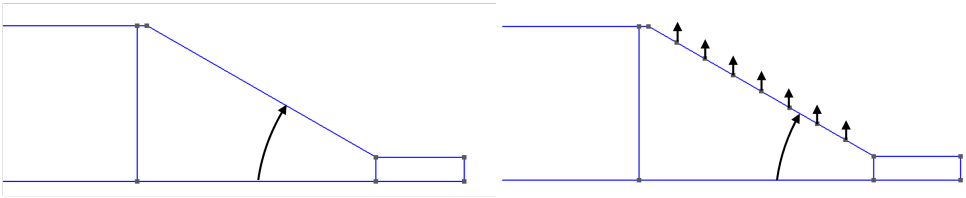

(a) Angle parametrization. (b) Combined spline parametrization.

Fig. 2: The two different geometry parameterizations used. Source: Authors own work

algorithm (Ragonneau, 2022; Ragonneau and Zhang, 2024). This algorithm uses a quadratic approximation of the objective function in every iteration. It is designed explicitly for derivative-free problems and can handle any constraints, so it is well-suited for our problem. The optimization algorithm then computes the values of the geometry parametrization for the next iteration. This optimization loop is then run for different process parameters; the results are shown in the next section.

4 Numerical Experiments

This section contains several numerical experiments: First, the results from the viscous model are presented for the angle optimization, followed by those for the spline-based parametrization. Section 4.2 presents the results for the viscoelastic material model, considering both the angle and spline parametrizations. The geometric parameters are listed in Table 1. For the viscous model, different outlet diameters were tested as well.

4.1 Temperature Dependent Viscous Model

Table 2 lists the parameters of the viscous model, explained in Section 2.1.1. The outlet diameter listed in Table 1 serves as the base case. First, the results from the

Table 2: Model parameters used for the numerical experiments of the viscous model (Lai, 2007).

Parameter	Value	Unit
Thermal diffusivity τ^*	1.009×10^5	Pa s
n	0.25	–
D_1	3.317×10^9	Pa s
T_{ref}	373	K
A_1	20.19	–
A_2	51.6	–

angle parametrization for different feeding rates are shown in Fig. 3. The feeding rate was adjusted from 0.6 mm/s to 2.8 mm/s. The optimal angle decreases for feeding

rates higher than 1.4 mm/s and reaches an optimal angle of around 30° for the highest feeding rate (Fig. 3a). It must be noted that higher feeding rates are not feasible for our model parameters, as the polymer then moves too fast through the nozzle to be fully melted at the outlet. In practice, this could lead to clogging of the nozzle. On the right, the percentage improvement of the pressure drop is plotted; for most feeding rates, the improvement is between 5% and 7%. For the higher feeding rates, the relative improvement (Eq. 12) decreases as the optimal angle approaches the initial angle of 30°.
The outlet diameter has a lower effect on the optimal angle (Fig. 4). For all tested outlet diameters, the optimal angle for minimizing the pressure loss is between 50° and 56°, and the relative improvement is around 5% to 5.5%.

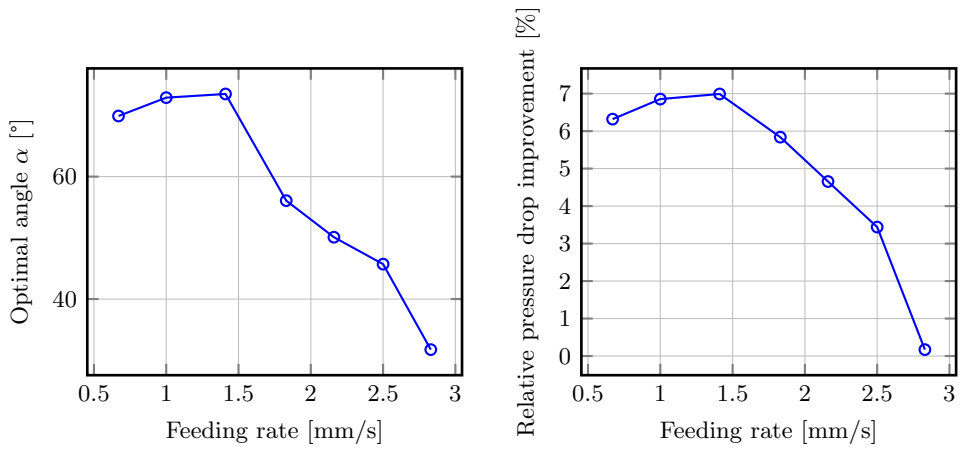

(a) Optimal angle

(b) Relative improvement of the pressure drop

Fig. 3: Optimal angle (a) and relative pressure drop improvement (b) for different feeding rates with a fixed outlet diameter of $d_{out} = 0.5$ mm. The geometry is shown in Fig. 1 and parameters are in Table 1. Source: Authors own work

In order to investigate if more complex geometries might yield further improvement, we now present the results from the spline parametrization. We ran the shape optimization using the same feeding rates and outlet diameters as in the angle optimization. In Fig. 5, a comparison of the relative improvement of the angle parametrization and the spline parametrization is shown. For all feeding rates and outlet diameters, the pressure drop improvement is slightly higher for the spline parametrization. Fig. 6 presents the resulting shapes for the cases with the highest and lowest feeding rates and outlet diameters. For the variation in outlet diameter (Fig. 6a and 6b), the spline geometry initially bends outward before narrowing more steeply near the outlet. In contrast, for the variation in feeding rate (Fig. 6c and 6d), the spline parametrization exhibits more

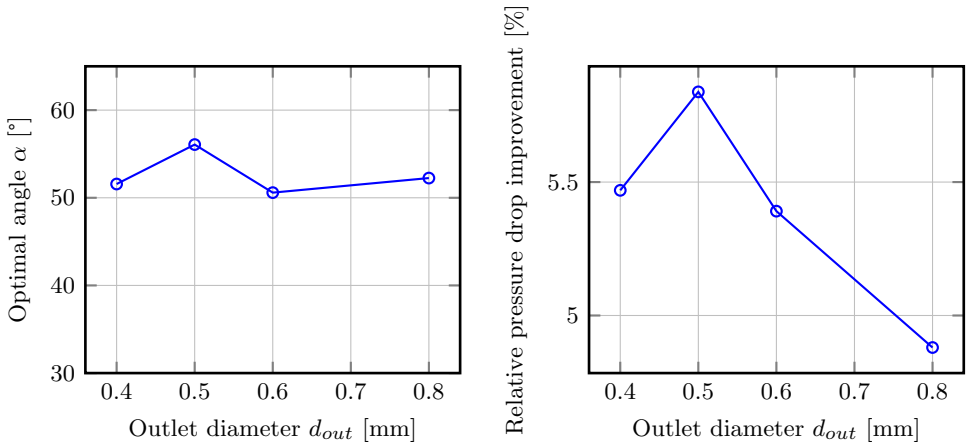

(a) Optimal angle (b) Relative improvement of the pressure drop

Fig. 4: Optimal angle (a) and relative pressure drop improvement (b) for different outlet diameter d_{out} with a fixed feeding rate of $u_{in} = 110$ mm/s. The geometry is shown in Fig. 1 and parameters are in Table 1. Source: Authors own work

minor geometric changes: at lower feeding rates, the shape bends outward, whereas at higher feeding rates, it bends inward. From a manufacturing perspective, it is unlikely that the relatively small reductions in pressure drop justify the increased production costs associated with more complex nozzle geometries.

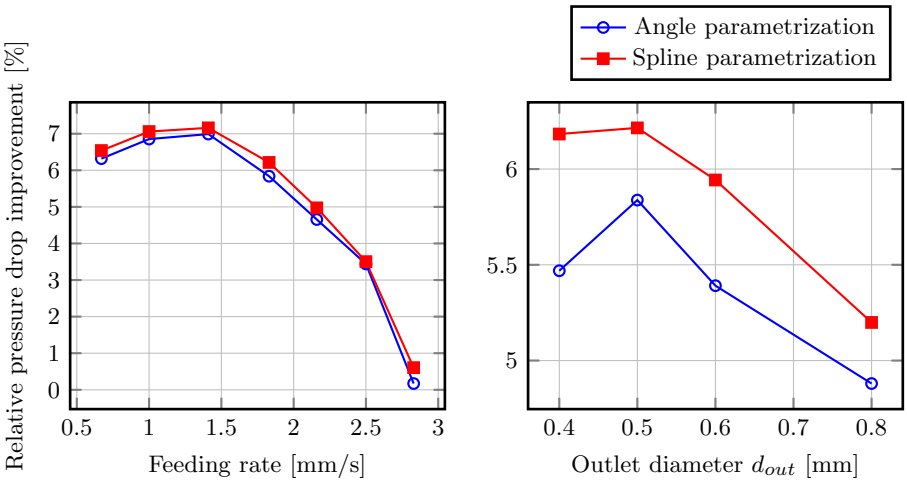

(a) Optimal angle (b) Relative improvement of the pressure drop

Fig. 5: Relative pressure drop improvement of the angle and spline parametrization for different feeding rates (a) and different outlet diameters (b). The geometry is shown in Fig. 1 and parameters are in Table 1. Source: Authors own work

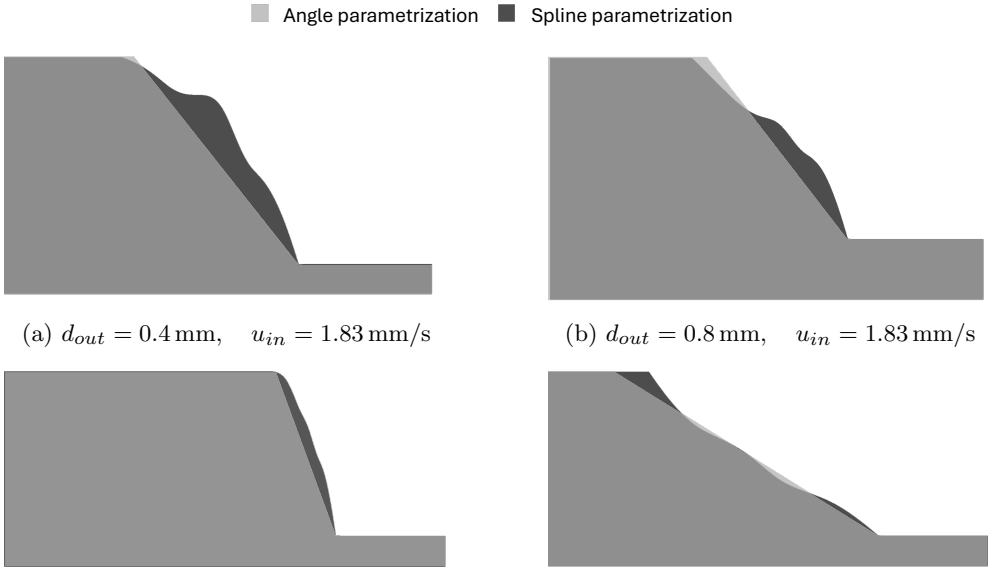

(a) $d_{out} = 0.4\,\mathrm{mm}, \quad u_{in} = 1.83\,\mathrm{mm/s}$

(b) $d_{out} = 0.8\,\mathrm{mm}, \quad u_{in} = 1.83\,\mathrm{mm/s}$

(c) $d_{out} = 0.5\,\mathrm{mm}, \quad u_{in} = 0.67\,\mathrm{mm/s}$

(d) $d_{out} = 0.5\,\mathrm{mm}, \quad u_{in} = 2.83\,\mathrm{mm/s}$

Fig. 6: Optimal shape for minimizing pressure drop for angle parametrization (light gray) and spline parametrization (dark gray) for different operating conditions. Source: Authors own work

4.2 Isothermal Viscoelastic Model

In this section, we present the results obtained with the viscoelastic model. It should be noted that the model is isothermal and formulated as a planar 2D model rather than an axisymmetric one. Table 3 shows the material parameters of the Giesekus model for PLA material, which are similar to the viscoelastic model parameters of PLA in (Schuller *et al.*, 2024a). The material parameters of PLA, the feeding rate, and the geometry lead to high Wi numbers, which are known to cause numerical difficulties (Keunings, 1986) and lead to the formation of large vortices. Continuation techniques are required to achieve convergence at high Wi numbers, where the relaxation time is gradually increased and the mobility factor is decreased. This procedure raises the computational cost by a factor of 10–20. Due to the increased computational cost, we ran the shape optimization only for different feeding rates and not for different outlet diameters.

Table 3: Material parameters used for the viscoelastic model

Parameter	Value	Unit
Relaxation time λ	0.2	1/s
Mobility factor α_G	0.05	-
Solvent viscosity ratio β	0.15	-
Total viscosity η	2000	Pa s
Density ρ	1250	kg/m^3

We performed the angle optimization for the viscoelastic model at four different inlet velocities, with the results shown in Fig. 7. The inlet velocities are higher than those used for the viscous model because, in the planar 2D formulation, the nozzle cross-section decreases only linearly. Consequently, the inlet velocity must be increased to achieve the same maximum outlet velocity. The initial guess for the optimizer is set to 50°. Across all cases, the optimal angle lies between 51° and 54.2°. The lowest value, 51.12°, is obtained for an inlet velocity of 10 mm/s. For both higher and lower inlet velocities, the optimal angle is slightly larger. The relative improvement ranges from 7.5% to 5.5%, decreasing with increasing feeding rates.
To better understand the flow inside the nozzle, we looked at the flow fields with the streamlines for the case with the inlet velocity of 10 mm/s (Fig. 8). For 30° and 50°, no vortices are present, but for 70° and 90°, a vortex appears. Due to the high Wi number with higher inlet velocities, the lip and corner vortex grow and merge into one vertex. This can be observed for the different inlet velocities from 5 mm/s (Fig. 9), 7.5 mm/s (Fig. 10), and 12.5 mm/s (Fig. 11) at the 70° angle. For each inlet velocity, the vortex is the largest at the 90° angle. The size of the vortex also affects the pressure drop; for inlet velocities up to 10 mm/s, the vortex for the 70° angle increases the pressure drop, but for the 90° angle, the pressure drop is slightly below the value for the 50° angle. The angle optimizer only found the local minimum at around 50°. The lower pressure drop for the 90° angle can be explained by the fact that the friction losses between the vortex and the main flow are lower than direct contact of the flow and the

wall. In practice, however, these recirculation areas should be avoided because they can promote backflow in the nozzle or lead to material degradation in the vortex. This issue could be addressed in future work by modifying the objective function to consider vortices. For the case with the highest inlet velocity of 12.5 mm/s, the pressure drop is higher for the 90° angle compared to 50°.
The spline-based shape optimization was only run for the feeding rate of 10 mm/s (Table 4). The optimal pressure loss could be slightly improved compared to the angle parametrization, which is the same as for the temperature-dependent viscous model.

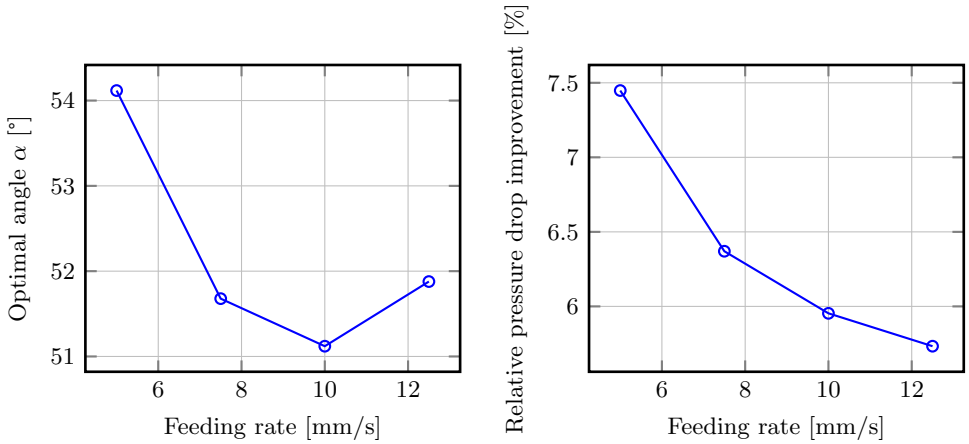

(a) Optimal angle (b) Relative improvement of the pressure drop

Fig. 7: Optimal angle (a) and relative pressure drop improvement (b) for different feeding rates of the viscoelastic material model with a fixed outlet diameter of $d_{out} = 0.5$ mm. The geometry is shown in Fig. 1 and parameters are in Table 3. Source: Authors own work

Table 4: Pressure loss Δp for the angle and spline paramertization for different feeding rates

Feeding rate	Angle paramertization	Spline parametrization
10 mm/s	0.945 96 MPa	0.945 24 MPa

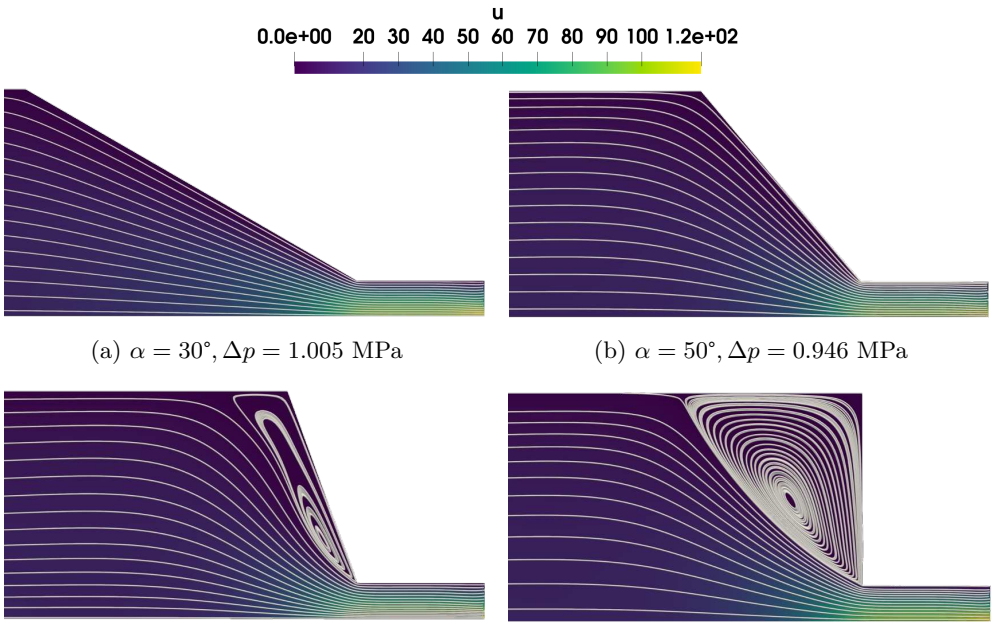

(a) $\alpha = 30°, \Delta p = 1.005$ MPa

(b) $\alpha = 50°, \Delta p = 0.946$ MPa

(c) $\alpha = 70°, \Delta p = 0.951$ MPa

(d) $\alpha = 90°, \Delta p = 0.944$ MPa

Fig. 8: Flow field of the velocity in x-direction (u) with the streamlines for four different contraction angles with a feeding rate of 10 mm/s. The operating conditions are listed in Table 3. Source: Authors own work

5 Discussion and Outlook

Our numerical experiments identified the optimal nozzle shapes for different material models and operating conditions. For the temperature-dependent model, the optimal shape is influenced primarily by the feeding rate, while the outlet diameter plays only a minor role. In contrast, for the viscoelastic model, the feeding rate exerts a weaker influence on the optimal geometry. The resulting shapes differ significantly between the two models, reflecting the distinct simplifications each makes in describing polymer behavior inside the nozzle. At present, it remains uncertain which model provides a more accurate representation of the actual flow. As future work, we plan to integrate both approaches into a temperature-dependent viscoelastic model in order to obtain more reliable predictions.

Across both models and all operating conditions, the spline-based shape parametrization provided only modest improvements compared to the simpler angle-based parametrization. Additionally, the resulting spline geometries are more complex and thus associated with higher manufacturing costs, which may outweigh the small performance gains.

Acknowledgments. The presented investigations were carried out at RWTH Aachen University within the framework of the Collaborative Research Centre SFB1120-236616214 “Bauteilpräzision durch Beherrschung von Schmelze und Erstarrung in Produktionsprozessen” and funded by the Deutsche Forschungsgemeinschaft (DFG, German Research Foundation) - 566317635. The sponsorship and support are gratefully acknowledged.
The authors also gratefully acknowledge the German Federal Ministry of Research, Technology and Space (BMFTR) and the state of North Rhine-Westphalia for supporting this work as part of the NHR funding.

Data Availability. The data and materials for this publication are available on request at the following link http://hdl.handle.net/21.11102/0adeb604-8a42-46b1-a734-85d6bc56fc16.

Appendix

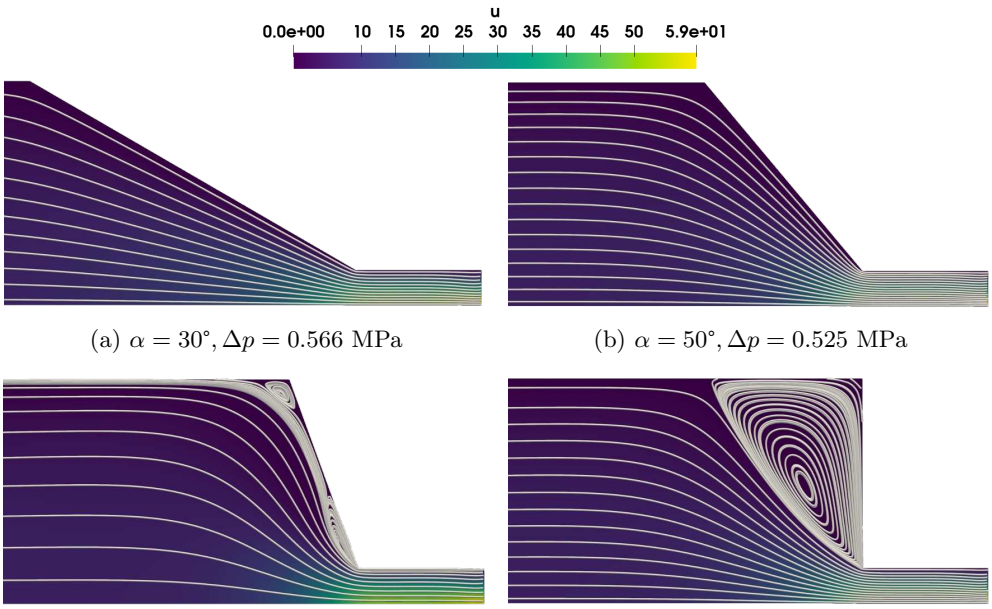

(a) $\alpha = 30°, \Delta p = 0.566$ MPa

(b) $\alpha = 50°, \Delta p = 0.525$ MPa

(c) $\alpha = 70°, \Delta p = 0.528$ MPa

(d) $\alpha = 90°, \Delta p = 0.518$ MPa

Fig. 9: Flow field of the velocity in x-direction (u) with the streamlines for four different contraction angles with a feeding rate of 5 mm/s. The operating conditions are listed in Table 3. Source: Authors own work

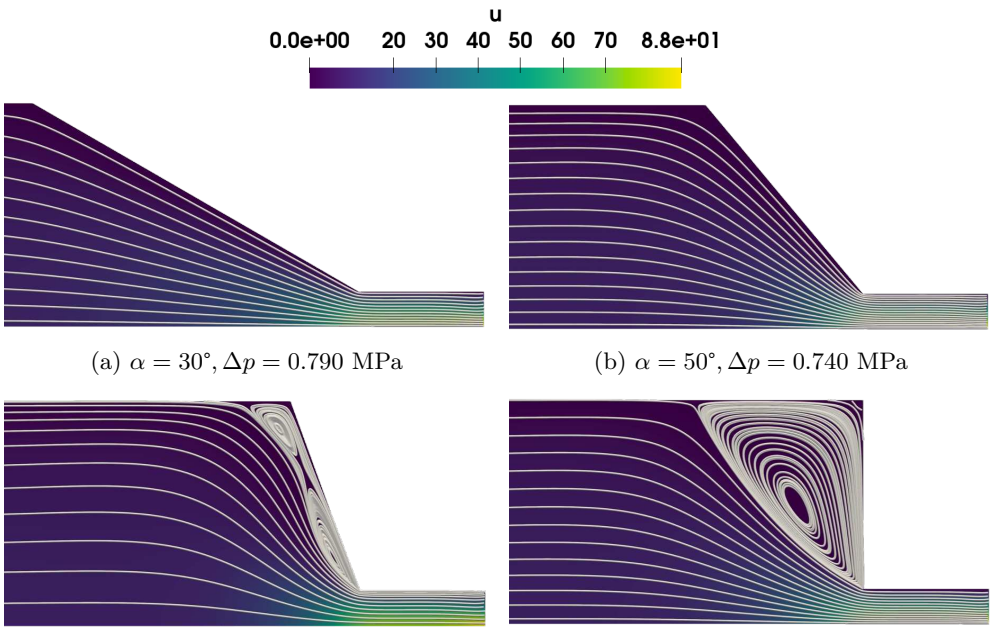

(a) $\alpha = 30°, \Delta p = 0.790$ MPa

(b) $\alpha = 50°, \Delta p = 0.740$ MPa

(c) $\alpha = 70°, \Delta p = 0.745$ MPa

(d) $\alpha = 90°, \Delta p = 0.735$ MPa

Fig. 10: Flow field of the velocity in x-direction (u) with the streamlines for four different contraction angles with a feeding rate of 7.5 mm/s. The operating conditions are listed in Table 3. Source: Authors own work

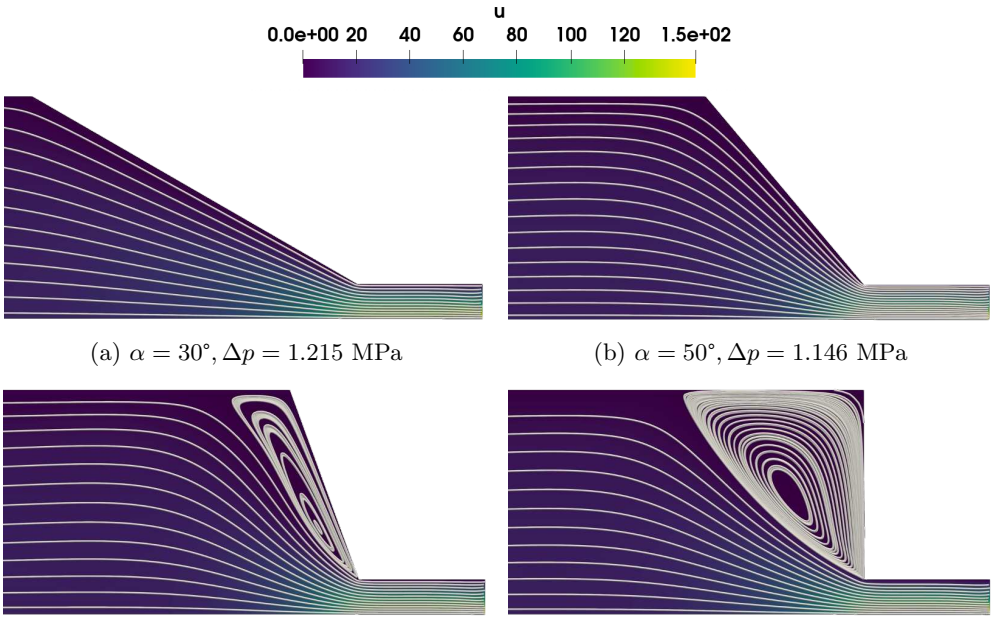

(a) $\alpha = 30°, \Delta p = 1.215$ MPa

(b) $\alpha = 50°, \Delta p = 1.146$ MPa

(c) $\alpha = 70°, \Delta p = 1.149$ MPa

(d) $\alpha = 90°, \Delta p = 1.149$ MPa

Fig. 11: Flow field of the velocity in x-direction (u) with the streamlines for four different contraction angles with a feeding rate of 12.5 mm/s. The operating conditions are listed in Table 3. Source: Authors own work

References

Anis A Ansari and M Kamil. Effect of print speed and extrusion temperature on properties of 3d printed pla using fused deposition modeling process. *Materials Today: Proceedings*, 45:5462–5468, 2021.

Hideyuki Azegami *et al. Shape optimization problems*. Springer, Singapore, 2020.

A Cano-Vicent, MM Tambuwala, SS Hassan, D Barh, AAA Aljabali, M Birkett, A Arjunan, and Á Serrano-Aroca. Fused deposition modelling: current status, methodology, applications and future prospects, addit. manuf. 47 (2021), 102378, 2021.

Morgane Chapelier, Robin Bouclier, and Jean-Charles Passieux. Spline-based specimen shape optimization for robust material model calibration. *Advanced Modeling and Simulation in Engineering Sciences*, 9(1):4, 2022.

Andrew R Conn, Katya Scheinberg, and Luis N Vicente. *Introduction to derivative-free optimization*. SIAM, 2009.

Christophe Geuzaine and Jean-François Remacle. Gmsh: A 3-d finite element mesh generator with built-in pre-and post-processing facilities. *International journal for numerical methods in engineering*, 79(11):1309–1331, 2009.

Kyriakos C Giannakoglou and Dimitrios I Papadimitriou. Adjoint methods for shape optimization. *Optimization and computational fluid dynamics*, pages 79–108, 2008.

Felipe A González. *Boundary-conforming finite-element methods applied to fused deposition modeling*. PhD thesis, Dissertation, Rheinisch-Westfälische Technische Hochschule Aachen, 2023, 2023.

Felipe A González, Stefanie Elgeti, Marek Behr, and Ferdinando Auricchio. A deforming-mesh finite-element approach applied to the large-translation and free-surface scenario of fused deposition modeling. *International Journal for Numerical Methods in Fluids*, 95(2):334–351, 2023.

Rasul Hajili and Mikail Temirel. Computational fluid dynamics (cfd) analysis of 3d printer nozzle designs. *Bitlis Eren Üniversitesi Fen Bilimleri Dergisi*, 13(4):1233–1246, 2024.

Abid Haleem, Vineet Kumar, and Lalit Kumar. Mathematical modelling & pressure drop analysis of fused deposition modelling feed wire. *Int. J. Eng. Technol*, 9(4): 2885–2894, 2017.

Xiaocong Han and David W Zingg. An adaptive geometry parametrization for aerodynamic shape optimization. *Optimization and Engineering*, 15(1):69–91, 2014.

Joe Hiemenz. 3d printing with fdm: How it works. *Stratasys Inc*, 1:1–5, 2011.

Onur Hıra, Senem Yücedağ, Shahrad Samankan, Övgü Yağız Çiçek, and Atakan Altınkaynak. Numerical and experimental analysis of optimal nozzle dimensions for fdm printers. *Progress in Additive Manufacturing*, 7(5):823–838, 2022.

Thomas Hofstaetter, Rodrigo Pimentel, David B Pedersen, Michael Mischkot, and Hans N Hansen. Simulation of a downsized fdm nozzle. In *COMSOL Conference 2015*, 2015.

Majid Hojjat, Electra Stavropoulou, and Kai-Uwe Bletzinger. The vertex morphing method for node-based shape optimization. *Computer Methods in Applied Mechanics and Engineering*, 268:494–513, 2014.

Antony Jameson. Aerodynamic shape optimization using the adjoint method. *Lectures at the Von Karman Institute, Brussels*, 2003.

Prashant Kaduba Kedare, SA Khan, and Harish Kumar. 3d printer nozzle design and its parameters: a systematic review. In *Proceedings of International Conference in Mechanical and Energy Technology: ICMET 2019, India*, pages 777–785. Springer, 2020.

Roland Keunings. On the high weissenberg number problem. *Journal of Non-Newtonian Fluid Mechanics*, 20:209–226, 1986.

Juliah Lai. Moldflow Material Testing Report, MAT2238, NatureWorks PLA. Moldflow Plastics Labs, 2007. URL https://www.natureworksllc.com.

Jeffrey Larson, Matt Menickelly, and Stefan M Wild. Derivative-free optimization methods. *Acta Numerica*, 28:287–404, 2019.

Chau Le, Tyler Bruns, and Daniel Tortorelli. A gradient-based, parameter-free approach to shape optimization. *Computer Methods in Applied Mechanics and Engineering*, 200(9-12):985–996, 2011.

Sarah Marion, Lucas Sardo, Thomas Joffre, and Franck Pigeonneau. First steps of the melting of an amorphous polymer through a hot-end of a material extrusion additive manufacturing. *Additive Manufacturing*, 65:103435, 2023. doi: 10.1016/j.addma.2023.103435.

Sarah Marion, Thomas Joffre, Julien Jaxel, and Franck Pigeonneau. Improved printability and electrical conductivity of carbon black polymer composite with a customized nozzle of material extrusion process. *Additive Manufacturing*, 79:103939, 2024. doi: 10.1016/j.addma.2023.103939.

Łukasz Miazio. Impact of print speed on strength of samples printed in fdm technology. *Agricultural Engineering*, 23, 2019.

Ray Tahir Mushtaq, Asif Iqbal, Yanen Wang, Mudassar Rehman, and Mohd Iskandar Petra. Investigation and optimization of effects of 3d printer process parameters on performance parameters. *Materials*, 16(9):3392, 2023.

VH Nguyen, TN Huynh, TP Nguyen, and TT Tran. Single and multi-objective optimization of processing parameters for fused deposition modeling in 3d printing technology. *International journal of automotive and mechanical engineering*, 17(1): 7542–7551, 2020.

Gaius Chukwuka Nzebuka, Chukwuzubelu Okenwa Ufodike, Al Mazedur Rahman, Chavous Maurice Gwynn, and Mohammad Faisal Ahmed. Numerical modeling of the effect of nozzle diameter and heat flux on the polymer flow in fused filament fabrication. *Journal of Manufacturing Processes*, 82:585–600, 2022a. doi: 10.1016/j.jmapro.2022.08.029.

Gaius Chukwuka Nzebuka, Chukwuzubelu Okenwa Ufodike, Al Mazedur Rahman, Chavous Maurice Gwynn, and Mohammad Faisal Ahmed. Numerical modeling of the effect of nozzle diameter and heat flux on the polymer flow in fused filament fabrication. *Journal of Manufacturing Processes*, 82:585–600, 2022b.

Simon Painchaud-Ouellet, Christophe Tribes, Jean-Yves Trépanier, and Dominique Pelletier. Airfoil shape optimization using a nonuniform rational b-splines parametrization under thickness constraint. *AIAA journal*, 44(10):2170–2178, 2006.

Sumit Paul. Finite element analysis in fused deposition modeling research: A literature review. *Measurement*, 178:109320, 2021.

Rhuan José Ribeiro Pereira, Fabricio Alves de Almeida, and Guilherme Ferreira Gomes. A multiobjective optimization parameters applied to additive manufacturing: Doe-based approach to 3d printing. In *Structures*, volume 55, pages 1710–1731. Elsevier, 2023.

David D Phan, Jeffrey S Horner, Zachary R Swain, Antony N Beris, and Michael E Mackay. Computational fluid dynamics simulation of the melting process in the fused filament fabrication additive manufacturing technique. *Additive Manufacturing*, 33:101161, 2020. doi: 10.1016/j.addma.2020.101161.

Franck Pigeonneau, D Xu, M Vincent, and J-F Agassant. Heating and flow computations of an amorphous polymer in the liquefier of a material extrusion 3d printer. *Additive Manufacturing*, 32:101001, 2020. doi: 10.1016/j.addma.2019.101001.

T. M. Ragonneau. *Model-Based Derivative-Free Optimization Methods and Software*. PhD thesis, Department of Applied Mathematics, The Hong Kong Polytechnic University, Hong Kong, China, 2022. URL https://theses.lib.polyu.edu.hk/handle/200/12294.

T. M. Ragonneau and Z. Zhang. COBYQA Version 1.1.2, 2024. URL https://www.cobyqa.com.

Luis Miguel Rios and Nikolaos V Sahinidis. Derivative-free optimization: a review of algorithms and comparison of software implementations. *Journal of Global Optimization*, 56(3):1247–1293, 2013.

Tomás Schuller, Paola Fanzio, and Francisco J Galindo-Rosales. Analysis of the importance of shear-induced elastic stresses in material extrusion. *Additive Manufacturing*, 57:102952, 2022. doi: 10.1016/j.addma.2022.102952.

Tomás Schuller, Paola Fanzio, and Francisco J Galindo-Rosales. Assessing nozzle flow dynamics in fused filament fabrication through the parametric map α- λ. *Physics of Fluids*, 36(3), 2024a.

Tomás Schuller, Maziyar Jalaal, Paola Fanzio, and Francisco J Galindo-Rosales. Optimal shape design of printing nozzles for extrusion-based additive manufacturing. *Additive Manufacturing*, 84:104130, 2024b.

Thomas W Sederberg and Scott R Parry. Free-form deformation of solid geometric models. In *Proceedings of the 13th annual conference on Computer graphics and interactive techniques*, pages 151–160, 1986.

Marcin P Serdeczny, Raphaël Comminal, Md Tusher Mollah, David B Pedersen, and Jon Spangenberg. Numerical modeling of the polymer flow through the hot-end in filament-based material extrusion additive manufacturing. *Additive Manufacturing*, 36:101454, 2020a. doi: 10.1016/j.addma.2020.101454.

Marcin P Serdeczny, Raphaël Comminal, David B Pedersen, and Jon Spangenberg. Experimental and analytical study of the polymer melt flow through the hot-end in material extrusion additive manufacturing. *Additive Manufacturing*, 32:100997, 2020b.

Marcin P Serdeczny, Raphaël Comminal, Md Tusher Mollah, David B Pedersen, and Jon Spangenberg. Viscoelastic simulation and optimisation of the polymer flow

through the hot-end during filament-based material extrusion additive manufacturing. *Virtual and Physical Prototyping*, 17(2):205–219, 2022. doi: 10.1080/17452759.2022.2028522.

Mohammad Shirmohammadi, Saeid Jafarzadeh Goushchi, and Peyman Mashhadi Keshtiban. Optimization of 3d printing process parameters to minimize surface roughness with hybrid artificial neural network model and particle swarm algorithm. *Progress in Additive Manufacturing*, 6(2):199–215, 2021.

I John Solomon, P Sevvel, and JJMTP Gunasekaran. A review on the various processing parameters in fdm. *Materials Today: Proceedings*, 37:509–514, 2021.

Chukwuzubelu Okenwa Ufodike and Gaius Chukwuka Nzebuka. Investigation of thermal evolution and fluid flow in the hot-end of a material extrusion 3d printer using melting model. *Additive Manufacturing*, 49:102502, 2022. doi: 10.1016/j.addma.2021.102502.

Jun Wang, Hang Hu, Ziyi Liu, Yuanyuan Shi, and Yizhe Huang. Optimization of 3d printing nozzle parameters and the optimal combination of 3d printer process parameters for engineering plastics with high melting points and large thermal expansion coefficients. *Materials*, 18(3):500, 2025.

Stefan Wittschieber, Leszek Demkowicz, and Marek Behr. Stabilized finite element methods for a fully-implicit logarithmic reformulation of the oldroyd-b constitutive law. *Journal of Non-Newtonian Fluid Mechanics*, 306:104838, 2022. doi: 10.1016/j.jnnfm.2022.104838.

Stefan Franz Wittschieber. *Robust finite element methods for viscoelastic constitutive laws in log-conformation form.* Dissertation, RWTH Aachen University (2023), Aachen.

Xuguang Xu, Huilin Ren, Shengyang Chen, Xiaofan Luo, Feihu Zhao, and Yi Xiong. Review on melt flow simulations for thermoplastics and their fiber reinforced composites in fused deposition modeling. *Journal of Manufacturing Processes*, 92:272–286, 2023. doi: 10.1016/j.jmapro.2023.02.039.

Xuguang Xu, Wanglin Qiu, Dongdong Wan, Jin Wu, Feihu Zhao, and Yi Xiong. Numerical modelling of the viscoelastic polymer melt flow in material extrusion additive manufacturing. *Virtual and Physical Prototyping*, 19(1):e2300666, 2024. doi: 10.1080/17452759.2023.2300666.

Jelena Žarko, Gojko Vladić, Magdolna Pál, and Sandra Dedijer. Influence of printing speed on production of embossing tools using fdm 3d printing technology. *Journal of graphic engineering and design*, 8(1):19–27, 2017.

Jie Zhang, Fankai Meng, and Eleonora Ferraris. Temperature gradient at the nozzle outlet in material extrusion additive manufacturing with thermoplastic filament. *Additive Manufacturing*, 73:103660, 2023. ISSN 2214-8604. doi: 10.1016/j.addma.2023.103660.